Research Square

Preprints are preliminary reports that have not undergone peer review.
They should not be considered conclusive, used to inform clinical practice,
or referenced by the media as validated information.

# Oxygen-Vacancy Engineering Coupled with In Situ Spinel Reconstruction Enables Fast Electronic and Ionic Transport in Li-Rich Layered Cathodes

**Wenxiao Su**
Lanzhou University of Technology
**Wangjun Feng**
wjfeng@lut.edu.cn

Lanzhou University of Technology
**Zhifeng Zhao**
Lanzhou University of Technology
**Qi Zhou**
Lanzhou University of Technology
**Guorong Liu**
Lanzhou University of Technology
**Yue Jian**
Lanzhou Institute of Technology

**Research Article**

**Keywords:** Lithium-rich manganese-based cathode (LMR), Acid surface treatment, Oxygen vacancy engineering, In situ spinel coating, Electrochemical performance enhancement

**Posted Date:** November 23rd, 2026

**DOI:** https://doi.org/10.21203/rs.3.rs-11690620/v1

**License:** This work is licensed under a Creative Commons Attribution 4.0 International License.
Read Full License

**Additional Declarations:** No competing interests reported.

# Abstract

Lithium-rich Mn-based cathodes possess exceptionally high energy-storage potential but suffer from severe voltage decay, sluggish reaction kinetics, and structural instability associated with lattice oxygen loss. Herein, a malic-acid-assisted surface engineering strategy is developed to simultaneously induce oxygen vacancies and an in-situ spinel reconstruction layer on $Li_{1.2}Mn_{0.54}Ni_{0.13}Co_{0.13}O_2$. Under optimized treatment conditions (pH = 2.5), a uniform ~ 30 nm spinel shell is formed, providing fast three-dimensional Li-ion transport channels and enhanced interfacial stability. Combined experimental investigations and density functional theory calculations reveal that oxygen vacancies not only facilitate the formation of the spinel phase but also trigger electronic structure reconfiguration. The introduced vacancies increase the electronic states near the Fermi level, eliminate the band gap, and promote metallic-like conductivity. Moreover, the Li-ion migration barrier is significantly reduced from 0.67 to 0.38 eV. COHP analysis demonstrates that this kinetic enhancement originates from the suppression of Li–O antibonding interactions and stabilization of the migration transition state. Owing to the synergistic effects of surface reconstruction and oxygen-vacancy engineering, the optimized LMR-2.5@1 cathode delivers 290.7 mAh $g^{-1}$ at 0.1 C and retains 85.7% of its capacity after 600 cycles at 1 C. This work provides an effective route for developing durable, high-performance Li-rich cathodes through coupled structural and electronic regulation.


# 1. Introduction

Shifting from traditional fossil fuels toward sustainable renewables demands immediate attention, where advancing robust and highly effective power storage technologies plays an indispensable role. Within this technological landscape, rechargeable lithium-ion cells dominate both electric mobility and mobile device markets. Their exceptional specific energy and extended operational lifespan make them prime contenders for grid-level applications. Satisfying the constantly growing global power requirements necessitates exploring innovative cathodic architectures delivering superior gravimetric capacities alongside reduced manufacturing expenses [1, 2].

Specifically, Li-rich Mn-based layered oxides (abbreviated as LMRs, formulated as $xLi_2MnO_3(1 - x)LiMO_2$, where M = Ni, Co, Mn, etc.) capture tremendous academic attention. They deliver extraordinary specific capacities exceeding 250 mAh $g^{-1}$ coupled with elevated operational potentials. Such outstanding metrics position these transition metal oxides as highly promising framework choices for future high-energy-density rechargeable batteries [3–5]. Nevertheless, practical deployment remains severely restricted by intrinsic physicochemical flaws. Repeated electrochemical cycling provokes profound lattice degradation, primarily driven by irreversible oxygen gas evolution, triggering rapid capacity decay alongside severe voltage suppression. Furthermore, the intrinsically sluggish electron transport and hindered ionic mobility yield unsatisfactory rate performances, obstructing any fast-charging practical implementations [6–8]. Countless researchers have devised diverse mitigation techniques to circumvent these obstacles, spanning from morphological tailoring [9–11] and elemental substitution [12–16] to protective shell application [17–20] and pre-activation methodologies [21–24]. Even with these

comprehensive efforts, major bottlenecks endure. Standard artificial layers like metal fluorides or simple oxides typically function as electrochemically inactive shields. Instead of promoting ionic percolation, they frequently elevate charge-transfer impedances. Moreover, crystallographic incompatibilities between foreign modifiers and the internal layered matrix provoke poor mechanical adhesion, ultimately causing severe cracking and subsequent peeling upon prolonged operation. Effectively engineering a dynamically active, seamlessly integrated exterior phase via electronic structure manipulation is still remarkably difficult. Therefore, inventing an innovative protocol capable of concurrently fortifying the anionic lattice, accelerating internal cation diffusion, and preserving overall morphological robustness constitutes an urgent research priority.

Herein, we introduces an easily scalable, targeted interfacial modification approach utilizing malic acid. This mild procedure synergistically integrates oxygen vacancy generation with the spontaneous epitaxial formation of a localized spinel overlayer. Distinct from traditional externally applied layers suffering from sluggish kinetics and mismatched lattices, the proposed chemical transformation facilitates the continuous growth of a highly crystalline spinel phase. Crucially, this newly formed region shares perfect crystallographic coherence with the underlying pristine host. Throughout the low-concentration acidic processing, targeted proton-for-lithium substitution yields a cation-depleted surface. Subsequent charge equilibrium necessities drive the partial conversion from tetravalent to trivalent manganese, simultaneously prompting the release of anionic species to form localized defects. The artificially introduced anionic vacancies play an indispensable dual role. Thermodynamically, they serve as initial nucleation sites, effectively depressing the activation energy required for the subsequent layered-to-spinel atomic rearrangement during thermal treatment. Electronically, they profoundly reconstruct the intrinsic band structure. Comprehensive spectroscopic evaluations combined with first-principles calculations verify the multifunctional nature of this reconstructed boundary. It successfully impedes detrimental gas evolution by reinforcing the atomic skeletal framework. Simultaneously, it establishes a three-dimensional pathway for rapid lithium intercalation while transforming the exterior from a sluggish semiconductor into a highly conductive metallic state, which sharply diminishes charge-transfer barriers. Ultimately, this comprehensive structural architecture remarkably upgrades both the mechanical longevity and the dynamic electrochemical profiles of the designed energy storage devices.

## 2. Experimental section

# 2.1 Material Synthesis

The carbonate precursor was synthesized via a co-precipitation method. $MnSO_4$, $NiSO_4$, and $CoSO_4$ were dissolved in deionized water with a molar ratio of 4:1:1 to obtain a mixed-metal solution (1.0 mol $L^{-1}$). An equimolar $Na_2CO_3$ solution was used as the precipitant, while $NH_4OH$ served as the chelating agent. The metal salt solution and $NH_4OH$ were simultaneously introduced into a four-neck reactor maintained at 55°C under continuous stirring. During the coprecipitation process, the feed rate of $Na_2CO_3$ solution was carefully regulated to stabilize the suspension pH at ~ 7.8. The formed solid phase was then retrieved,

repeatedly rinsed with deionized water to remove residual ions, and subsequently dried. The dried precursor was subsequently mixed with $Li_2CO_3$ using a Li/(Mn + Ni+Co) molar ratio of 1.5 via wet ball milling, followed by solvent evaporation under stirring. The obtained mixture was first preheated at 500°C for 5 h in air to promote solid-state diffusion, and then calcined at 850°C for 12 h to complete phase formation. The resulting layered oxide $Li_{1.2}Mn_{0.54}Ni_{0.13}Co_{0.13}O_2$ was designated as LMR.

## 2.2 Acid Treatment Procedure

For surface modification, 0.5 g of LMR powder was dispersed in 50 mL deionized water and ultrasonicated for 10 min. A malic acid solution (0.5 g $mL^{-1}$) was then added dropwise under stirring until the suspension reached target pH values of 3.0, 2.5, or 2.0. After stirring for 1 h, the solids were separated, washed thoroughly, and dried. The collected powders were subsequently annealed in air at 500°C for 2 h. The treated samples were labeled LMR-3.0@1, LMR-2.5@1, and LMR-2.0@1 according to the corresponding pH values. For comparison, a control sample (LMR-W@1) was prepared using the same dispersion, ultrasonication, and heat-treatment procedures without the addition of malic acid.

## 2.3 Material Characterization

Phase composition and purity were examined by X-ray diffraction (TD-3700, Dandong Tongda) from 10° to 80° at 2° $min^{-1}$. Surface chemical states were analyzed using X-ray photoelectron spectroscopy (ESCALAB 250Xi, Thermo Fisher). Sample morphology and internal microstructure were observed by SEM (JSM-6701F, JEOL) and TEM (JEM-2100F, JEOL), respectively. Piezoelectric responses were measured with an atomic force microscope (Bruker MultiMode 8-HR), while oxygen vacancies were detected by room-temperature electron paramagnetic resonance spectroscopy (Bruker EMXplus).

## 2.4 Electrochemical Performance Testing

For electrochemical evaluation, composite cathodes were prepared by dispersing the active material, acetylene black, and polyvinylidene fluoride in N-methyl-2-pyrrolidone at a mass ratio of 8:1:1. The resulting slurry was cast onto aluminum foil, vacuum dried at 110°C for 12 h, and punched and pressed into 12 mm disks. CR2025 coin cells were assembled in an argon-filled glovebox with $H_2O$ and $O_2$ concentrations below 0.1 ppm. Lithium foil served as both the counter and reference electrode, while Celgard 2500 was used as the separator. The electrolyte consisted of 1.0 mol $L^{-1}$ $LiPF_6$ dissolved in ethylene carbonate, dimethyl carbonate, and diethyl carbonate at a volume ratio of 1:1:1. Galvanostatic charge–discharge and intermittent titration measurements were conducted from 2.0 to 4.8 V using a CT2001A battery testing system. Electrochemical impedance spectra were recorded with a CS350H workstation.

## 2.5 Theoretical calculations

Density functional theory (DFT) simulations were carried out within the Vienna Ab initio Simulation Package (VASP) framework [25–27]. The exchange–correlation interaction was treated using the Perdew–Burke–Ernzerhof (PBE) functional under the generalized gradient approximation (GGA) [28], while the ion–electron interaction was described by the projector augmented wave (PAW) method [29].

Brillouin zone integrations were performed using a Monkhorst–Pack k-point sampling scheme, employing a 12 × 8 × 12 mesh for structural relaxation and a denser 25 × 16 × 25 grid for accurate electronic structure calculations. A plane-wave cutoff energy of 550 eV was applied throughout. Structural optimization included full relaxation of both lattice parameters and atomic coordinates until the total energy convergence reached $1 \times 10^{-5}$ eV, with residual atomic forces reduced below 0.01 eV $Å^{-1}$.

To precisely capture the pronounced localized magnetic moments originating from the manganese 3d orbitals, spin-polarized configurations were universally enforced across all computational simulations. Preceding the geometric relaxation, initial magnetic states were defined by allocating 5 μB to individual Mn centers, while lithium and oxygen species were initialized as completely non-magnetic (0 μB). A conjugate gradient minimization algorithm was deployed to concurrently optimize atomic coordinates alongside macroscopic lattice parameters (both shape and volume). This iterative convergence was strictly terminated once the residual Hellmann-Feynman forces acting on all constituent atoms diminished below the 0.01 eV $Å^{-1}$ threshold. Following the comprehensive structural relaxation within the postulated ferromagnetic framework, the overall magnetic moment of the simulation cell stabilized at approximately 12.0 μB. This macroscopic magnitude yields an average local moment of ~ 3.0 μB per manganese site, firmly substantiating the preservation of robust spin-polarized electronic characteristics under the prescribed theoretical conditions.

# 3. Results and Discussion

Figure 1 shows the X-ray diffraction (XRD) patterns of the pristine and acid-treated LMR samples. All samples exhibit the characteristic peaks of a layered α-$NaFeO_2$-type structure (space group R3m, PDF#87-1563), along with superstructure peaks originating from the $Li_2MnO_3$ component (space group C2/m) in the 20°–25° (2$\theta$) range. The overall similarity of the patterns before and after acid treatment indicates that the layered structure remains intact and that the modification primarily affects the near-surface region. The enlarged view of the (003) and (104) peaks in panel (a) shows that with increasing acid concentration, both peaks shift to lower angles, indicating an overall lattice expansion. Rietveld refinement results (Table 1) show that for the pristine LMR, the layered phase (R-3m) has lattice parameters a = 2.8493 Å, c = 14.2141 Å, and c/a = 4.9886. After malic acid treatment (LMR-2.5@1), the a-axis slightly increases to 2.8509 Å, while the c-axis expands more significantly to 14.2313 Å, resulting in an increased c/a ratio of 4.9918. The shift of the (003) and (104) reflections toward lower Bragg angles indicates lattice expansion, particularly along the c-axis. This anisotropic change is associated with acid-induced surface reconstruction. Specifically, $H^+/Li^+$ exchange generates a Li-deficient surface layer; charge compensation leads to partial reduction of $Mn^{4+}$ to $Mn^{3+}$, whose larger ionic radius induces Jahn–Teller distortion [30, 31]. Consequently, Mn–O bonds are elongated along the c direction, resulting in increased interlayer spacing. The formation of oxygen vacancies further enhances this reduction-induced expansion [32]. Upon annealing, the reconstructed surface transforms into a spinel phase coherently interfaced with the layered bulk, and the resulting interfacial strain additionally contributes to the peak shift [33].

Table 1
Rietveld refinement parameters obtained from XRD data of LMR and LMR-2.5@1.

| Sample | Phase | Space group | *a* (Å) | *c* (Å) | *c*/*a* | $R_{wp}$ (%) | $\chi^2$ |
|---|---|---|---|---|---|---|---|
| LMR | Layered | $R\bar{3}m$ | 2.8493 | 14.2141 | 4.9886 | 4.05 | 1.52 |
| | $Li_2MnO_3$ | *C2/m* | 4.9449 | 5.0103 | - | | |
| LMR-2.5@1 | Layered | $R\bar{3}m$ | 2.8509 | 14.2313 | 4.9918 | 11.27 | 1.71 |
| | $Li_2MnO_3$ | *C2/m* | 4.9513 | 5.0193 | - | | |

To elucidate the impact of malic acid concentration on surface reconstruction, the morphologies of LMR samples treated under varying pH conditions were characterized by scanning electron microscopy (SEM), as shown in Fig. 2a-c. All samples maintained their spherical particle morphology with diameters of approximately 3–10 μm, confirming that the acid leaching process did not compromise the overall microstructure. However, with increasing acid concentration under fixed treatment duration, the particle surfaces became progressively smoother, exhibiting features indicative of a reconstructed layer without residual etching marks. Energy-dispersive X-ray spectroscopy (EDS) mapping (Fig. 2d-r) revealed a homogeneous distribution of all elements, suggesting that the acid treatment did not induce notable element segregation. Quantitative analysis based on the full EDS spectra (Fig. 2s-y) further confirmed the preserved bulk composition, though minor variations in transition metal ratios were observed, attributable to differential leaching rates among metallic constituents. Notably, a significant decrease in surface oxygen content was detected with intensified acid leaching. The pristine sample (LMR) exhibited an oxygen content of 75.8%, consistent with the theoretical value for the layered $Li_{1.2}Mn_{0.56}Ni_{0.13}Co_{0.13}O_2$ phase. This value decreased to 69.2% for LMR-2.5@1 and further dropped to 60% for LMR-2.0@1. This trend is attributed to the progressive replacement of surface $Li^+$ by $H^+$ from malic acid, forming an unstable hydroxylated layer that decomposes during subsequent annealing, releasing $H_2O$ or $O_2$ and creating oxygen vacancies. These vacancies facilitate transition metal migration and trigger the transformation of the surface structure into a spinel-type phase (e.g., $LiM_2O_4$) with a lower oxygen stoichiometry [34, 35].

To verify the formation of a spinel structure on the surface of LMR materials after acid leaching, transmission electron microscopy (TEM) was performed on various samples. Structural analysis was carried out by applying Fourier transform (FFT) to lattice fringe images and interpreting the corresponding diffraction patterns, as illustrated in Fig. 3. As shown in Fig. 3(b, e, h-i, m-n), the surface region of the LMR-2.5@1 sample exhibits single-crystal diffraction spots consistent with the ordered spinel phase (space group $P4_332$), indicating the formation of an approximately 30 nm thick ordered spinel layer. In contrast, the LMR-2.0@1 sample (Figure. 3(c, f, j-o, k-p)) displays not only an underlying

ordered spinel phase but also an outermost layer (~ 15 nm thick) identified as a tetragonal spinel phase ($I4_1/amd$).

The presence of distinct spinel phases in LMR-2.0@1 can be attributed to the increased concentration of malic acid, which elevates the $H^+$ content in the leaching solution. Since the ion exchange rate between $H^+$ and metal ions is directly proportional to proton concentration [36], a moderate $H^+$ concentration facilitates a uniform exchange process, resulting in an ordered spinel layer. However, when the $H^+$ concentration becomes excessively high, the ion exchange rate accelerates, leading to significant $Li^+$ depletion in the outermost region of the material. This promotes the formation of a $LiMn_3O_4$-like tetragonal spinel phase [34], which, unfortunately, exhibits a lower Mn oxidation state. This makes the tetragonal spinel phase susceptible to disproportionation reactions, causing Mn dissolution [37]. As a result, this phase can be considered undesirable, as it compromises the electrochemical stability of the material by promoting side reactions with the electrolyte, ultimately impairing battery performance. Thickness analysis based on TEM images revealed that the ordered spinel layer in LMR-2.5@1 is approximately 30 nm thick, while in LMR-2.0@1, it extends to about 80 nm, with an additional 15 nm-thick tetragonal spinel layer on top. These findings further emphasize the impact of acid leaching on spinel formation. It is crucial to note that the acid leaching-induced spinel structure differs significantly from the “spinel-inlaid-in-layered-matrix” model proposed by Gu et al. [38], which arises from the structural degradation of layered LMR materials. In the inlaid model, the spinel phase disrupts the layered framework, obstructing the two-dimensional $Li^+$ transport channels. In contrast, the spinel phase formed through acid leaching grows epitaxially on the layered host, maintaining structural compatibility and promoting a stable interface [39]. This ordered surface spinel not only facilitates the creation of continuous three-dimensional $Li^+$ transport pathways, thereby enhancing ion transport kinetics, but also acts as a protective barrier, isolating the bulk LMR material from direct electrolyte contact. This significantly mitigates parasitic reactions, improving both the structural stability and electrochemical performance of the material. Thus, the formation of the spinel phase via acid leaching represents a promising strategy for improving the overall performance and longevity of the battery.

Figure 4 shows the Raman and EPR responses of the different samples. In the Raman spectra (Fig. 4a), characteristic bands at 495 and 602 $cm^{-1}$ are assigned to the Eg (O–M–O) and A1g (M–O) vibrational modes of the layered R3m phase, respectively. Additional features at 350 and 395 $cm^{-1}$ are associated with the $Li_2MnO_3$ component [40]. A distinct band at 675 $cm^{-1}$, corresponding to the Eg mode of the spinel structure [41], becomes progressively stronger with increasing acid treatment severity, indicating that lower pH conditions favor the growth of a thicker spinel reconstruction layer. Notably, LMR-2.0@1 exhibits the most prominent spinel-related signal, in agreement with TEM observations. The EPR spectra (Fig. 4b) further confirm the presence of oxygen vacancies. While pristine LMR shows no obvious signal, all treated samples display a broad symmetric resonance centered at g = 2.0057, characteristic of $F^+$ centers, arising from oxygen vacancies trapping a single electron [42]. The intense peak observed for LMR-2.5@1 confirms that acid leaching introduces a high concentration of oxygen vacancies. These results are in full agreement with the Raman and TEM analyses, collectively demonstrating that the acid

treatment simultaneously generates oxygen vacancies and induces a surface spinel phase. The synergistic effect between oxygen vacancies and the spinel coating is responsible for the improved structural stability and electrochemical performance.

To clarify the acid-induced surface reconstruction of LMR, X-ray photoelectron spectroscopy (XPS) was conducted to probe the evolution of surface chemical states (Fig. 5). In the O 1s spectra (Fig. 5b), three components located at ≈ 529.2, 531.3, and 533.2 eV are assigned to M–O bonds, lattice oxygen, and surface carbonate/hydroxyl species ($CO_3^{2-}$/$OH^-$), respectively [43, 44]. Compared with pristine LMR, the treated samples exhibit a noticeable decrease in the lattice oxygen contribution, indicating the formation of oxygen-deficient regions. This behavior originates from $H^+$/$Li^+$ exchange during acid exposure, which produces a hydroxylated surface layer that decomposes upon annealing, releasing gaseous species ($H_2O$ and/or $O_2$) and leaving oxygen vacancies. Meanwhile, the M–O peak shifts to higher binding energy, suggesting the development of a spinel-like surface phase with strengthened metal–oxygen interactions, which helps suppress further oxygen loss [45].

The Mn 3s spectra (Fig. 5c) provide insight into the Mn valence state through the multiplet splitting ($\Delta E_s$) [46]. Pristine LMR shows a $\Delta E$ of 4.38 eV, corresponding to an average Mn valence of ≈ + 3.88. After malic acid treatment (LMR-2.5@1), ΔE increases to 4.61 eV, accompanied by a decrease in average Mn valence to ≈ + 3.77; a further slight reduction to ≈ + 3.76 is observed for LMR-2.0@1. This trend indicates progressive Mn reduction with increasing treatment strength, consistent with the formation of a reconstructed surface layer.

Further evidence is obtained from the Mn 2p spectra (Fig. 5d), which can be deconvoluted into two spin–orbit doublets corresponding to $Mn^{3+}$ (642.0/653.2 eV) and $Mn^{4+}$ (643.6/654.8 eV). Quantitative analysis reveals that the $Mn^{4+}$ fraction decreases from 83.0% in pristine LMR to 58.2% in LMR-2.0@1, confirming enhanced $Mn^{4+}$ reduction and increased oxygen vacancy concentration under stronger acid conditions. In contrast, fitting of the Co 2p and Ni 2p spectra (Fig. 5e,f) shows only minor variations in $Co^{3+}$ and $Ni^{2+}$ contents, indicating that Mn plays a dominant role in the surface reconstruction and primarily drives spinel formation.

Based on the above analysis, the acid-induced surface reconstruction mechanism of LMR can be summarized as follows. In malic acid solution, $Li^+$ is extracted from the surface, generating lithium vacancies. Charge compensation is achieved through partial oxidation of lattice oxygen ($O^{2-} \rightarrow O^-/O_2$), leading to oxygen vacancy formation. Meanwhile, neighboring $Mn^{4+}$ ions are reduced to $Mn^{3+}$, whose larger ionic radius induces local Jahn–Teller distortion and forms a metastable surface layer. Upon subsequent annealing, thermally activated cation migration allows transition metal ions to occupy Li sites, resulting in the in situ transformation of the surface into a spinel phase (Fig. 3). The generated oxygen vacancies not only act as nucleation centers for spinel formation but also stabilize the oxygen framework, thereby suppressing irreversible oxygen release.

The electrochemical properties of the samples were systematically investigated (Fig. 6). As shown in the rate performance (Fig. 6a), pristine LMR delivers a discharge capacity of ~ 284 mAh $g^{-1}$ at 0.1C, but suffers from rapid decay as current density increases, indicating sluggish kinetics associated with poor ionic/electronic transport. In comparison, the acid-treated samples exhibit markedly improved rate behavior, which is attributed to the formation of a spinel-like surface layer that enables 3D $Li^+$ diffusion pathways. The initial charge–discharge profiles at 0.1C (Fig. 6b) show that pristine LMR delivers 259.0 mAh $g^{-1}$, whereas LMR-2.5@1 reaches 290.7 mAh $g^{-1}$ and LMR-2.0@1 achieves 284.9 mAh $g^{-1}$, corresponding to a 12.2% enhancement for the optimal sample. Notably, a new discharge plateau appears at ~ 2.7 V in the treated electrodes, a characteristic feature of spinel-type redox behavior [47], confirming in situ surface reconstruction from an electrochemical perspective. The first-cycle differential capacity (dQ/dV) profiles (Fig. 6c) further reveal the reaction pathways. Pristine LMR shows anodic peaks at ~ 4.2 V ($Ni^{2+}/Ni^{4+}$ and $Co^{3+}/Co^{4+}$) and a high-voltage feature at 4.5–4.6 V related to oxygen activation from $Li_2MnO_3$. By contrast, LMR-2.5@1 exhibits additional redox peaks at ~ 2.8 and 3.0 V, assigned to the $Mn^{3+}/Mn^{4+}$ couple in the spinel phase, directly confirming the formation of an electrochemically active spinel network. Meanwhile, the high-voltage oxygen redox signal becomes more stabilized, suggesting suppressed irreversible oxygen evolution. Rate-dependent dQ/dV curves (Fig. 6d) show that LMR-2.5@1 retains well-defined redox features even at high current densities, indicating improved kinetic robustness. Overall, the moderate acid treatment (pH ≈ 2.5) achieves an optimal balance between spinel layer formation and oxygen vacancy concentration, leading to enhanced rate capability, higher capacity, and improved redox reversibility, consistent with the structural and surface analyses presented above.

The effect of the surface spinel coating on electrochemical stability was evaluated by long-term cycling tests conducted at 1 C (Fig. 7). LMR-2.5@1 exhibits outstanding stability, retaining 85.7% of its initial capacity (229.5 mAh $g^{-1}$) after 600 cycles, whereas LMR-2.0@1 fails after ~ 400 cycles due to severe side reactions. The average discharge voltage decays rapidly in the first 200 cycles (Process 1), then slows considerably (Process 2). This behavior is attributed to initial irreversible oxygen release and $Mn^{4+}$ reduction to $Mn^{3+}$, which lowers the operating potential. Once the cations stabilize in a spinel/rock-salt framework, further decay is retarded. dQ/dV analysis (Figs. 7b, 7c) confirms that Process 1 involves irreversible layered-to-spinel transformation (peaks shift to lower voltages), while in Process 2 the peak shifts are subdued, indicating a more stable structural evolution. Notably, LMR-2.5@1 maintains a Coulombic efficiency > 99% throughout cycling, whereas LMR-2.0@1 shows a fluctuating decline after ~ 300 cycles, correlating with parasitic peaks in dQ/dV. This confirms that moderate acid treatment (pH = 2.5) generates an ordered spinel layer of appropriate thickness, effectively stabilizing the interface and suppressing side reactions. In contrast, excessive treatment (pH ≤ 2.0) induces a detrimental tetragonal spinel phase (I41/amd), where $Mn^{3+}$-driven Jahn–Teller distortion and disproportionation trigger electrolyte decomposition. Thus, the acid-induced surface spinel reconstruction significantly enhances cycling stability, but the outcome critically depends on the structure and thickness of the reconstructed layer.

The effect of malic acid treatment on the electrochemical kinetics of lithium-rich manganese-based (LMR) materials was evaluated by cyclic voltammetry (CV), as shown in Fig. 8. During the first three cycles (Fig. 8a–e), all samples display two main anodic peaks at ~ 4.2 and ~ 4.6 V. These are associated with the $Ni^{2+}/Ni^{4+}$ and $Co^{3+}/Co^{4+}$ redox couples in the layered structure, as well as the activation of the $Li_2MnO_3$ component accompanied by lattice oxygen oxidation ($O^{2-} \rightarrow O^{n-}$), respectively. [40]. Notably, the acid-treated samples display a distinct redox couple at ~ 2.9 V (anodic) and ~ 2.7 V (cathodic), which serves as a prominent electrochemical fingerprint of the spinel phase. This couple represents the $Li^+$ intercalation within the spinel structure coupled with the $Mn^{3+}/Mn^{4+}$ redox reaction [48]. A comparative analysis of the first and third cycle CV curves (Figs. 8f and g) reveals a clear concentration-dependent trend: the intensities of the spinel-associated peaks at 2.9 V/2.7 V scale with the acid concentration, indicating a higher degree of surface phase transformation. Concurrently, the oxidation peak at 4.6 V and the subsequent reduction peaks at 3.2 V and 4.4 V are significantly enhanced in the modified samples, particularly for LMR-2.5@1. This suggests that the in-situ generated surface spinel layer not only provides additional electrochemical capacity but also acts as a structural scaffold that stabilizes the lattice oxygen. By mitigating irreversible oxygen release, this heterostructure fosters a more favorable environment for reversible anionic redox reactions.

To systematically investigate the effect of surface-reconstructed spinel structures on the electrochemical kinetics of LMR materials, fresh button cells with varying compositions were subjected to electrochemical impedance spectroscopy (EIS) under open-circuit voltage (Fig. 9a). In the impedance spectra, the high-frequency semicircle is predominantly governed by the cell's ohmic resistance ($R_s$) and charge transfer resistance ($R_{ct}$), whereas the low-frequency diagonal reflects the lithium-ion diffusion impedance in the electrode (Warburg impedance). By fitting the spectra using an equivalent circuit model in conjunction with Equations (1) and (2), the lithium-ion diffusion coefficient ($D_{Li+}$) was further determined [49]. The $R_s$, $R_{ct}$, and $D_{Li+}$ values for all samples are summarized in Table 2.

The lithium-ion diffusion coefficient ($D_{Li^+}$) at the open-circuit potential was subsequently determined according to Eq. 1.

$$\mathrm{D}=\frac{\mathrm{R}^2\mathrm{T}^2}{2\mathrm{A}^2\mathrm{n}^4\mathrm{F}^4\mathrm{C}^2\sigma^2}$$

1

The relationship between the real part of the impedance and the angular frequency in the Warburg region was analyzed based on Eq. 2.

$$\mathrm{Z}\prime=\mathrm{R}_\mathrm{s}+\mathrm{R}_\mathrm{ct}+\sigma\omega^{-\frac{1}{2}}$$

2

The results (Fig. 9b) reveal that increasing malic acid concentration leads to a marked decrease in charge transfer resistance accompanied by an increase in lithium-ion diffusion coefficient, indicating that thickening the surface spinel layer effectively lowers the energy barrier for lithium-ion extraction. This behavior can be attributed to the superior conductivity of the spinel phase relative to the layered structure, as well as the formation of in-situ three-dimensional (3D) lithium-ion pathways within the surface spinel, which significantly enhances lithium-ion extraction kinetics [41]. These findings highlight that tuning the thickness of the surface spinel layer is an effective strategy to optimize the electrochemical performance of LMR materials.

Table 2
The ohmic resistance ($R_s$), charge transfer resistance ($R_{ct}$), and lithium-ion conductivity ($D_{Li^+}$) derived from EIS data fitting of different samples.

| **Samples** | **LMR** | **LMR-W@1** | **LMR-3.0@1** | **LMR-2.5@1** | **LMR-2.0@1** |
|---|---|---|---|---|---|
| $R_s$ (Ω) | 0.859 | 1.069 | 1.054 | 0.984 | 1.201 |
| $R_{ct}$ (Ω) | 537.3 | 415.9 | 337.0 | 230.1 | 198.4 |
| $D_{Li}^+$ ($cm^2\ s^{-1}$) | $6.049\times10^{-16}$ | $6.726\times10^{-16}$ | $9.355\times10^{-16}$ | $1.354\times10^{-15}$ | $8.701\times10^{-16}$ |

To gain deeper insight into the role of acid-induced oxygen vacancies in enhancing the electrochemical performance of Li-rich Mn-based cathodes, density functional theory (DFT) calculations were performed to investigate their electronic structure and Li-ion diffusion behavior. As shown in Fig. 10a,b, pristine LMR exhibits a nearly zero density of states (DOS) at the Fermi level and a band gap of approximately 2.11 eV, indicating typical semiconducting behavior with pronounced spin polarization. Such an electronic structure is associated with the intrinsically poor electronic conductivity and sluggish charge-transfer kinetics of the pristine material. After introducing oxygen vacancies, the DOS at the Fermi level increases significantly, accompanied by the disappearance of spin polarization (Fig. 10c) and the downward shift of the conduction band minimum, leading to band-gap closure (Fig. 10d). These results demonstrate that oxygen vacancies act as electron donors, transforming the material from a semiconductor into a metallic-like conductor. Meanwhile, the reduced spin polarization is consistent with the increased $Mn^{3+}$ content observed by XPS, confirming that the partial reduction of $Mn^{4+}$ to $Mn^{3+}$ plays a crucial role in the oxygen-vacancy-induced electronic reconstruction. Therefore, oxygen vacancies effectively enhance electronic conductivity and reduce charge-transfer resistance, thereby improving reaction kinetics and contributing to superior rate capability, Coulombic efficiency, and cycling stability.

As shown in Fig. 10e-10f, the calculated diffusion energy barrier for the pristine structure is 0.67 eV, indicating a relatively sluggish Li migration process governed by a rigid oxygen framework. In contrast, the introduction of oxygen vacancies significantly reduces the diffusion barrier to 0.38 eV, suggesting a markedly enhanced Li-ion mobility. Such a substantial reduction in migration barrier can be attributed to the local structural and electronic reconstruction induced by oxygen vacancies. The removal of lattice oxygen effectively weakens the electrostatic constraints of the surrounding oxygen sublattice, leading to

a more flexible migration channel and a stabilized transition state along the Li diffusion pathway. As a result, the energy penalty associated with Li hopping is significantly alleviated, accounting for the improved diffusion kinetics.

To further understand the origin of this kinetic enhancement, crystal orbital Hamilton population (COHP) analysis was carried out to probe the Li–O bonding characteristics (Fig. 10. g–h). The integrated COHP values (–ICOHP) slightly decrease from 0.94 eV in the pristine structure to 0.91 eV in the oxygen-deficient system, indicating a modest weakening of the overall Li–O bonding interaction. More importantly, the energy-resolved COHP profiles reveal a redistribution of antibonding states near the Fermi level upon oxygen vacancy formation. In the pristine structure, noticeable antibonding contributions persist in the vicinity of the Fermi level, which increase the energetic cost of Li migration. By contrast, these antibonding states are partially suppressed and redistributed in the oxygen-deficient structure, effectively lowering the energetic penalty for Li displacement.

This electronic reconfiguration suggests that the enhanced Li mobility does not primarily originate from a uniform weakening of Li–O bonds, but rather from a localized stabilization of the migration transition state. The oxygen vacancies reduce the antibonding interactions along the diffusion pathway, thereby lowering the saddle-point energy and facilitating Li-ion hopping. Combined with the diffusion barrier results, these findings demonstrate that oxygen vacancy engineering simultaneously modulates the lattice flexibility and electronic structure, synergistically promoting Li-ion transport.

Overall, the results indicate that acid-induced oxygen vacancies serve as an effective strategy to enhance Li-ion diffusion kinetics in Li-rich cathode materials by stabilizing the migration transition state and optimizing Li–O electronic interactions, rather than simply disrupting the lattice framework.

# Conclusion

In summary, a dual-functional surface modification strategy was developed for Li-rich layered oxide $Li_{1.2}Mn_{0.54}Ni_{0.13}Co_{0.13}O_2$ through a facile and scalable malic-acid treatment. By optimizing the solution acidity (pH = 2.5), an approximately 30 nm-thick spinel reconstruction layer was generated on the particle surface, accompanied by the formation of abundant oxygen vacancies. The cooperative effects of surface phase reconstruction and defect engineering effectively overcome the intrinsic limitations of Li-rich cathodes. Experimental characterization combined with first-principles calculations reveals the underlying enhancement mechanism. The reconstructed spinel phase provides fast three-dimensional Li-ion transport channels and mitigates interfacial degradation associated with oxygen release during cycling. Simultaneously, oxygen-vacancy formation induces partial $Mn^{4+}$ reduction and triggers significant electronic structure reconfiguration. Density functional theory calculations demonstrate that oxygen vacancies increase the electronic states near the Fermi level and eliminate the band gap, promoting a transition from semiconducting to metallic-like behavior. As a result, electron transport is substantially improved and charge-transfer resistance is reduced. More importantly, oxygen vacancies play a decisive role in facilitating Li-ion migration. The calculated diffusion barrier decreases markedly

from 0.67 eV for pristine LMR to 0.38 eV after vacancy introduction. COHP analysis further indicates that this kinetic improvement is not simply caused by weakened Li–O bonding; instead, it originates from the suppression of Li–O antibonding states near the Fermi level, which stabilizes the migration transition state and lowers the saddle-point energy along the diffusion pathway. Therefore, oxygen vacancies simultaneously optimize the electronic environment and local lattice flexibility, leading to accelerated Li-ion transport. Benefiting from these synergistic effects, the optimized LMR-2.5@1 electrode delivers a high discharge capacity of 290.7 mAh $g^{-1}$ at 0.1 C and retains 85.7% of its initial capacity after 600 cycles at 1 C. This study demonstrates that coupling oxygen-vacancy regulation with in-situ spinel reconstruction is an effective approach for simultaneously enhancing electronic conductivity, Li-ion diffusion kinetics, and structural stability, providing a viable pathway toward high-performance and commercially relevant Li-rich Mn-based cathode materials.

## Declarations

# Conflicts of Interest

The authors declare that they have no known competing financial interests or personal relationships that could have appeared to influence the work reported in this paper.

# Author Contribution

Wenxiao Su: Conceptualization, Methodology, Investigation, Data curation, Formal analysis, Visualization, Writing-original draft. Zhifeng Zhao: Software, Methodology, Formal analysis, Investigation (DFT calculations and COMSOL multiphysics simulations). Guorong Liu: Investigation (in situ XRD and PFM characterization), Validation, Data curation. Yue Jian: Investigation (HRTEM/STEM characterization and electrochemical measurements), Resources. Qi Zhou: Methodology, Resources, Supervision, Funding acquisition, Writing-review & editing. Wangjun Feng: Conceptualization, Project administration, Supervision, Funding acquisition, Resources, Writing-review & editing. All authors have read and approved the final version of the manuscript.

# Acknowledgements

This work is supported by the National Natural Science Foundation of China (No. 12464039); Incubation Program of Excellent Doctoral Dissertation-Lanzhou University of Technology; The Scientific Research Project of the Education Department of Gansu Province (No.2026B-247).

## CRediT authorship contribution statement

Wenxiao Su: Conceptualization, Methodology, Investigation, Data curation, Formal analysis, Visualization, Writing-original draft. Zhifeng Zhao: Software, Methodology, Formal analysis, Investigation (DFT calculations and COMSOL multiphysics simulations). Guorong Liu: Investigation (in situ XRD and PFM characterization), Validation, Data curation. Yue Jian: Investigation (HRTEM/STEM characterization and electrochemical measurements), Resources. Qi Zhou: Methodology, Resources, Supervision, Funding acquisition, Writing-review & editing. Wangjun Feng: Conceptualization, Project administration, Supervision, Funding acquisition, Resources, Writing-review & editing. All authors have read and approved the final version of the manuscript.

## References


1. (2025) Humanity needs to diversify its lithium sources. Nature 637:1021–1022. https://doi.org/10.1038/d41586-025-00213-0
2. Link S, Schneider L, Stephan A et al (2025) Feasibility of meeting future battery demand via domestic cell production in Europe. Nat Energy 10:526–534. https://doi.org/10.1038/s41560-025-01722-y
3. Jin Y, Zhao Z, Ren P et al (2024) Recent Advances in Oxygen Redox Activity of Lithium-Rich Manganese-Based Layered Oxides Cathode Materials: Mechanism, Challenges and Strategies. Adv Energy Mater 14:2402061. https://doi.org/10.1002/aenm.202402061
4. Yang Z, Gao L, Li Z et al (2025) Advances and Challenges of Lithium-Rich Manganese-Based Cathode Materials for All-Solid-State. Batteries ChemistryEurope 3:e202500148. https://doi.org/10.1002/ceur.202500148
5. Han Y, Wang G, Ren X et al (2025) High specific-energy lithium-rich manganese-based layered oxide cathodes: key challenges, modification strategies and future prospects. New Carbon Mater 40:597–620. https://doi.org/10.1016/S1872-5805(25)60996-6
6. Liu T, Liu J, Li L et al (2022) Origin of structural degradation in Li-rich layered oxide cathode. Nature 606:305–312. https://doi.org/10.1038/s41586-022-04689-y
7. Worku BE, Geng H, Ning Y et al (2025) Li-rich Mn-based cathode materials for next-generation Batteries: Degradation mechanisms, mitigation strategies, and advances toward solid-state batteries. Mater Today Energy 53:102015. https://doi.org/10.1016/j.mtener.2025.102015
8. Jin L, Du G, Liu P et al (2026) Voltage Decay and Capacity Loss in Lithium-Rich Manganese Oxide Cathodes: Atomic Origins, Mesoscopic Heterogeneities, and Macroscopic Evolution. Adv Mater 38:e21529. https://doi.org/10.1002/adma.202521529
9. Chen H, Xia X, Ma J (2024) Comprehensive Review of Li-Rich Mn-Based Layered Oxide Cathode Materials for Lithium-Ion Batteries: Theories, Challenges, Strategies and Perspectives. Chemsuschem 17:e202401120. https://doi.org/10.1002/cssc.202401120
10. Luo D, Shi P, Fang S et al (2017) Unraveling the effect of exposed facets on voltage decay and capacity fading of Li-rich layered oxides. J Power Sources 364:121–129. https://doi.org/10.1016/j.jpowsour.2017.07.078

11. Li J, Xu C, Zhao J et al (2018) Li-rich nanoplates of $Li_{1.2}Ni_{0.13}Co_{0.13}Mn_{0.54}O_2$ layered oxide with exposed {010} planes as a high-performance cathode for lithium-ion batteries. J Alloys Compd 734:301–306. https://doi.org/10.1016/j.jallcom.2017.10.285
12. Luo Z (2025) A Review on Element Doping in Li-Rich Cathode Materials for Lithium-Ion Batteries. E3S Web Conf 606:02009. https://doi.org/10.1051/e3sconf/202560602009
13. Choi A, Lim J, Kim H et al (2018) Site-Selective In Situ Electrochemical Doping for Mn-Rich Layered Oxide Cathode Materials in Lithium-Ion Batteries. Adv Energy Mater 8:1702514. https://doi.org/10.1002/aenm.201702514
14. Zou L, Li J, Liu Z et al (2019) Lattice doping regulated interfacial reactions in cathode for enhanced cycling stability. Nat Commun 10:3447. https://doi.org/10.1038/s41467-019-11299-2
15. Yan W, Xie Y, Jiang J et al (2018) Enhanced Rate Performance of Al-Doped Li-Rich Layered Cathode Material via Nucleation and Post-solvothermal Method. ACS Sustainable Chem Eng 6:4625–4632. https://doi.org/10.1021/acssuschemeng.7b03634
16. Dong S, Zhou Y, Hai C et al (2020) Understanding electrochemical performance improvement with Nb doping in lithium-rich manganese-based cathode materials. J Power Sources 462:228185. https://doi.org/10.1016/j.jpowsour.2020.228185
17. Yao Y, Zhang Z, Zheng Y et al (2025) Recent advances in coating strategies for lithium-rich manganese-based layered oxide cathodes. J Energy Storage 134:118132. https://doi.org/10.1016/j.est.2025.118132
18. Fu C, Zhou Y, Shen G et al (2025) Constructing LiF@spinel dual shell to suppress interfacial side reactions of Li-rich cathode materials. Energy Mater Devices 3:9370065. https://doi.org/10.26599/EMD.2025.9370065
19. Kang Y, Liang Z, Zhao Y et al (2020) Large-scale synthesis of lithium- and manganese-rich materials with uniform thin-film Al2O3 coating for stable cathode cycling. Sci China Mater 63:1683–1692. https://doi.org/10.1007/s40843-020-1327-8
20. Zheng J, Yang Z, Wang P et al (2018) Multiple Linkage Modification of Lithium-Rich Layered Oxide $Li_{1.2}Mn_{0.54}Ni_{0.13}Co_{0.13}O_2$ for Lithium Ion Battery. ACS Appl Mater Interfaces 10:31324–31329. https://doi.org/10.1021/acsami.8b09256
21. Lei T, Cao G, Shi X et al (2025) Enhancing the performance of Li-rich oxide cathodes through multifunctional surface engineering. J Power Sources 640:236717. https://doi.org/10.1016/j.jpowsour.2025.236717
22. Sun G, Yu F-D, Que L-F et al (2019) Local electronic structure modulation enhances operating voltage in Li-rich cathodes. Nano Energy 66:104102. https://doi.org/10.1016/j.nanoen.2019.104102
23. Li Y, Xie L, Zheng Z et al (2020) Hybridizing $Li@Mn_6$ and $Sb@Ni_6$ superstructure units to tune the electrochemical performance of Li-rich layered oxides. Nano Energy 77:105157. https://doi.org/10.1016/j.nanoen.2020.105157
24. Wu J, Han C, Yang H et al (2025) Organic weak acid pretreatment enables surface-engineered Li-rich cathodes with suppressed voltage decay and enhanced kinetics. Solid State Ionics 432:117051.

https://doi.org/10.1016/j.ssi.2025.117051

25. Kresse G, Furthmüller J (1996) Efficiency of ab-initio total energy calculations for metals and semiconductors using a plane-wave basis set. Comput Mater Sci 6:15–50. https://doi.org/10.1016/0927-0256(96)00008-0
26. Kresse G, Furthmüller J (1996) Efficient iterative schemes for *ab initio* total-energy calculations using a plane-wave basis set. Phys Rev B 54:11169–11186. https://doi.org/10.1103/PhysRevB.54.11169
27. Kresse G, Joubert D (1999) From ultrasoft pseudopotentials to the projector augmented-wave method. Phys Rev B 59:1758–1775. https://doi.org/10.1103/PhysRevB.59.1758
28. Perdew JP, Burke K, Ernzerhof M (1997) Generalized Gradient Approximation Made Simple. Phys Rev Lett 78:1396–1396. https://doi.org/10.1103/PhysRevLett.78.1396
29. Blöchl PE (1994) Projector augmented-wave method. Phys Rev B 50:17953–17979. https://doi.org/10.1103/PhysRevB.50.17953
30. Liu S, Wang B, Zhang X et al (2021) Reviving the lithium-manganese-based layered oxide cathodes for lithium-ion batteries. Matter 4:1511–1527. https://doi.org/10.1016/j.matt.2021.02.023
31. Li Q, Ning D, Wong D et al (2022) Improving the oxygen redox reversibility of Li-rich battery cathode materials via Coulombic repulsive interactions strategy. Nat Commun 13:1123. https://doi.org/10.1038/s41467-022-28793-9
32. Nakamura T, Gao H, Ohta K et al (2019) Defect chemical studies on oxygen release from the Li-rich cathode material $Li_{1.2}Mn_{0.6}Ni_{0.2}O_{2-\delta}$. J Mater Chem A 7:5009–5019. https://doi.org/10.1039/C8TA12484A
33. Li J, Klöpsch R, Stan MC et al (2011) Synthesis and electrochemical performance of the high voltage cathode material $Li[Li_{0.2}Mn_{0.56}Ni_{0.16}Co_{0.08}]O_2$ with improved rate capability. J Power Sources 196:4821–4825. https://doi.org/10.1016/j.jpowsour.2011.01.006
34. Huang Y, Dong Y, Li S et al (2021) Lithium Manganese Spinel Cathodes for Lithium-Ion Batteries. Adv Energy Mater 11:2000997. https://doi.org/10.1002/aenm.202000997
35. Fehse M, Etxebarria N, Otaegui L et al (2022) Influence of Transition-Metal Order on the Reaction Mechanism of LNMO Cathode Spinel: An *Operando* X-ray Absorption Spectroscopy Study. Chem Mater 34:6529–6540. https://doi.org/10.1021/acs.chemmater.2c01360
36. Sun C, Xu L, Chen X et al (2018) Sustainable recovery of valuable metals from spent lithium-ion batteries using DL-malic acid: Leaching and kinetics aspect. Waste Manag Res 36:113–120. https://doi.org/10.1177/0734242X17744273
37. Zhu X, Meng F, Zhang Q et al (2020) $LiMnO_2$ cathode stabilized by interfacial orbital ordering for sustainable lithium-ion batteries. Nat Sustain 4:392–401. https://doi.org/10.1038/s41893-020-00660-9
38. Gu M, Belharouak I, Zheng J et al (2013) Formation of the Spinel Phase in the Layered Composite Cathode Used in Li-Ion Batteries. ACS Nano 7:760–767. https://doi.org/10.1021/nn305065u

39. He J, Ma H, Zhang H et al (2020) Promoting the Electrochemical Performance of Li-Rich Layered $Li_{1.2}$ $(Ni_{1/6}$ $Co_{1/6}$ $Mn_{4/6})_{0.8}O_2$ with the In Situ Transformed Allogenic Spinel Phase. ACS Sustainable Chem Eng 8:2215–2225. https://doi.org/10.1021/acssuschemeng.9b05664
40. Celeste A, Brescia R, Gigli L et al (2023) Unravelling structural changes of the $Li_{1.2}Mn_{0.54}Ni_{0.13}Co_{0.13}O_2$ lattice upon cycling in lithium cell. Mater Today Sustain 21:100277. https://doi.org/10.1016/j.mtsust.2022.100277
41. Yang Z, Zhou H, Bao Z et al (2019) Enhanced rate capability and cycling stability of lithium-rich cathode material $Li_{1.2}Ni_{0.2}Mn_{0.6}O_2$ via $H_3PO_4$ pretreating and accompanying $Li_3PO_4$ coating. J Mater Sci: Mater Electron 30:19493–19504. https://doi.org/10.1007/s10854-019-02315-8
42. Martínez-Arias A, Soria J, Conesa JC et al (1995) NO reaction at surface oxygen vacancies generated in cerium oxide. J Chem Soc Faraday Trans 91:1679–1687. https://doi.org/10.1039/FT9959101679
43. Li W, Zhao B, Bai J et al (2023) Sulfuretted Li- and Mn-rich cathode material with epitaxial spinel stabilizer for ultra-long cycle Li-ion battery. Chem Eng J 454:140398. https://doi.org/10.1016/j.cej.2022.140398
44. Zheng H, Hu Z, Liu P et al (2020) Surface Ni-rich engineering towards highly stable $Li_{1.2}Mn_{0.54}Ni_{0.13}Co_{0.13}O_2$ cathode materials. Energy Storage Mater 25:76–85. https://doi.org/10.1016/j.ensm.2019.10.029
45. He J, Hua W, Missiul A et al (2021) Phosphoric acid and thermal treatments reveal the peculiar role of surface oxygen anions in lithium and manganese-rich layered oxides. J Mater Chem A 9:264–273. https://doi.org/10.1039/D0TA07371G
46. Galakhov VR, Demeter M, Bartkowski S et al (2002) Mn 3 s exchange splitting in mixed-valence manganites. Phys Rev B 65:113102. https://doi.org/10.1103/PhysRevB.65.113102
47. Song B, Liu H, Liu Z et al (2013) High rate capability caused by surface cubic spinels in Li-rich layer-structured cathodes for Li-ion batteries. Sci Rep 3:3094. https://doi.org/10.1038/srep03094
48. Vanaphuti P, Azhari L, Ma X et al (2022) Upgrading the Performance and Stability of Lithium, Manganese-Rich Layered Oxide Cathodes with Combined-Formic Acid and Spinel Coating Treatment. Batteries Supercaps 5:e202100377. https://doi.org/10.1002/batt.202100377
49. Ho C, Raistrick ID, Huggins RA (1980) Application of A-C Techniques to the Study of Lithium Diffusion in Tungsten Trioxide Thin Films. J Electrochem Soc 127:343–350. https://doi.org/10.1149/1.2129668

# Footnotes

*** Corresponding author**: Address: School of Science, Lanzhou University of Technology, Gansu Lanzhou 730050, China. E-mail address: wjfeng@lut.edu.cn (W.J. Feng).

* **Corresponding author**: Address: School of Materials Science and Engineering, Lanzhou University of Technology, Gansu Lanzhou 730050, China. E-mail address: zhouxq301@sina.com(Q. Zhou).

# Figures

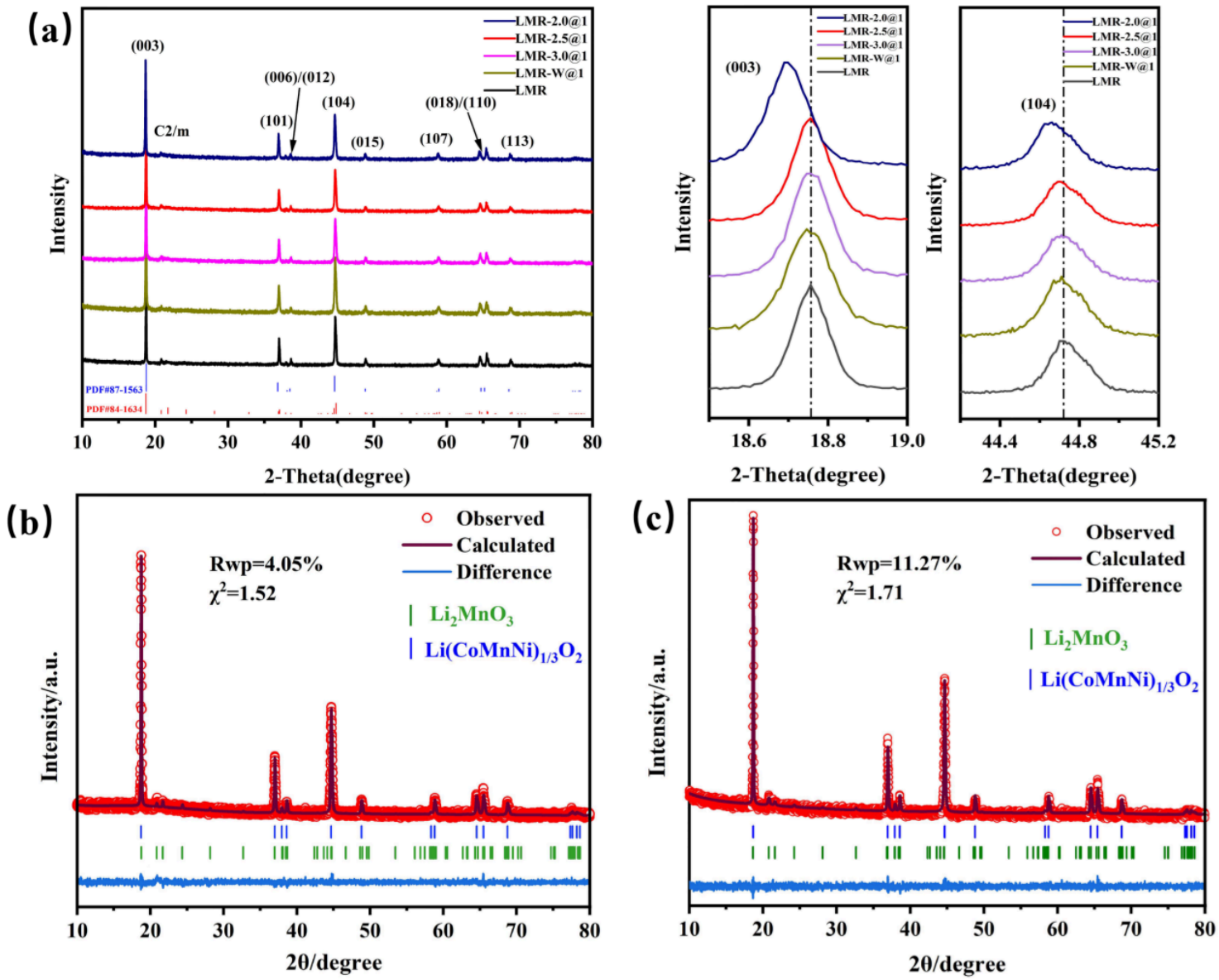
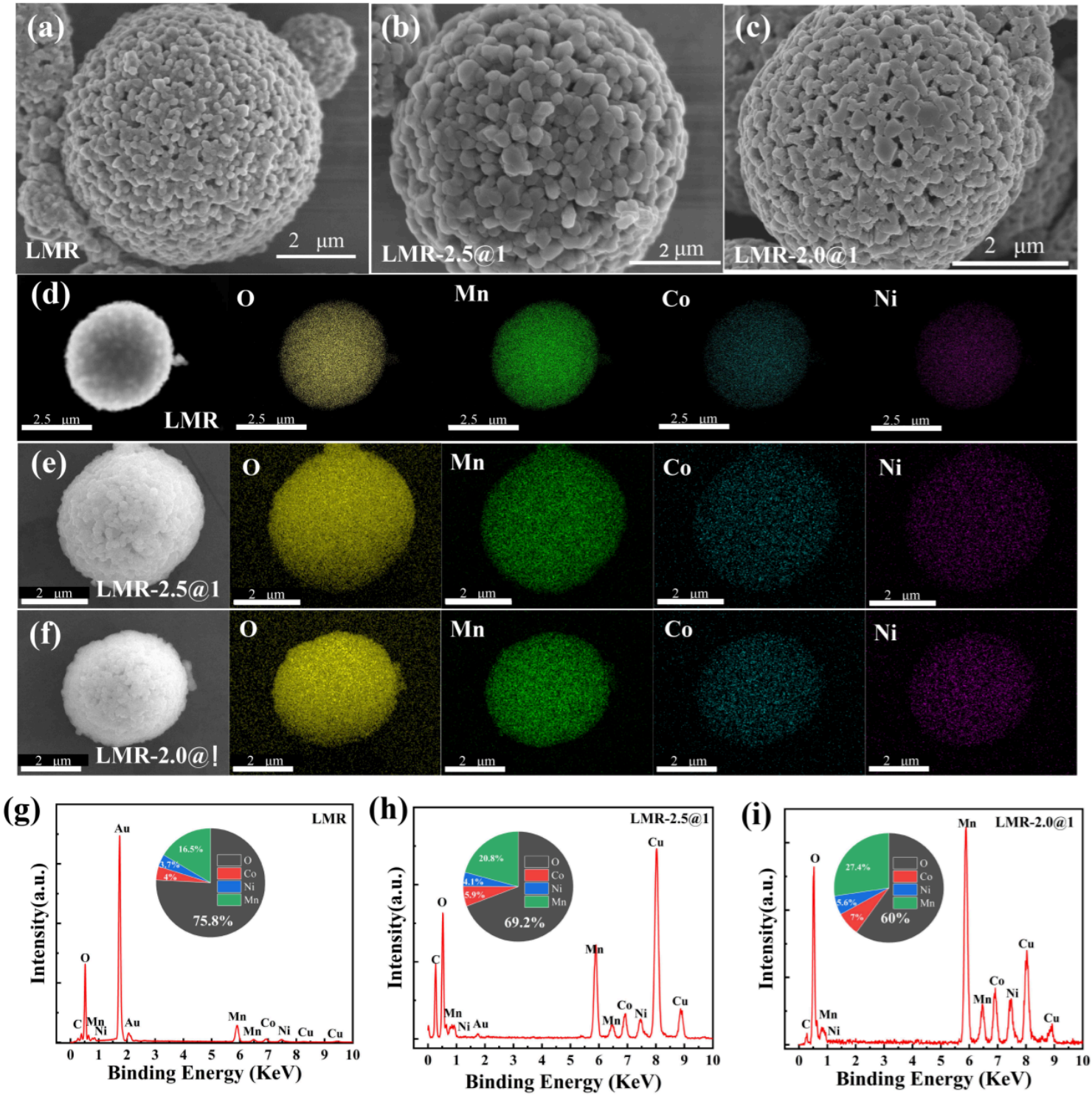


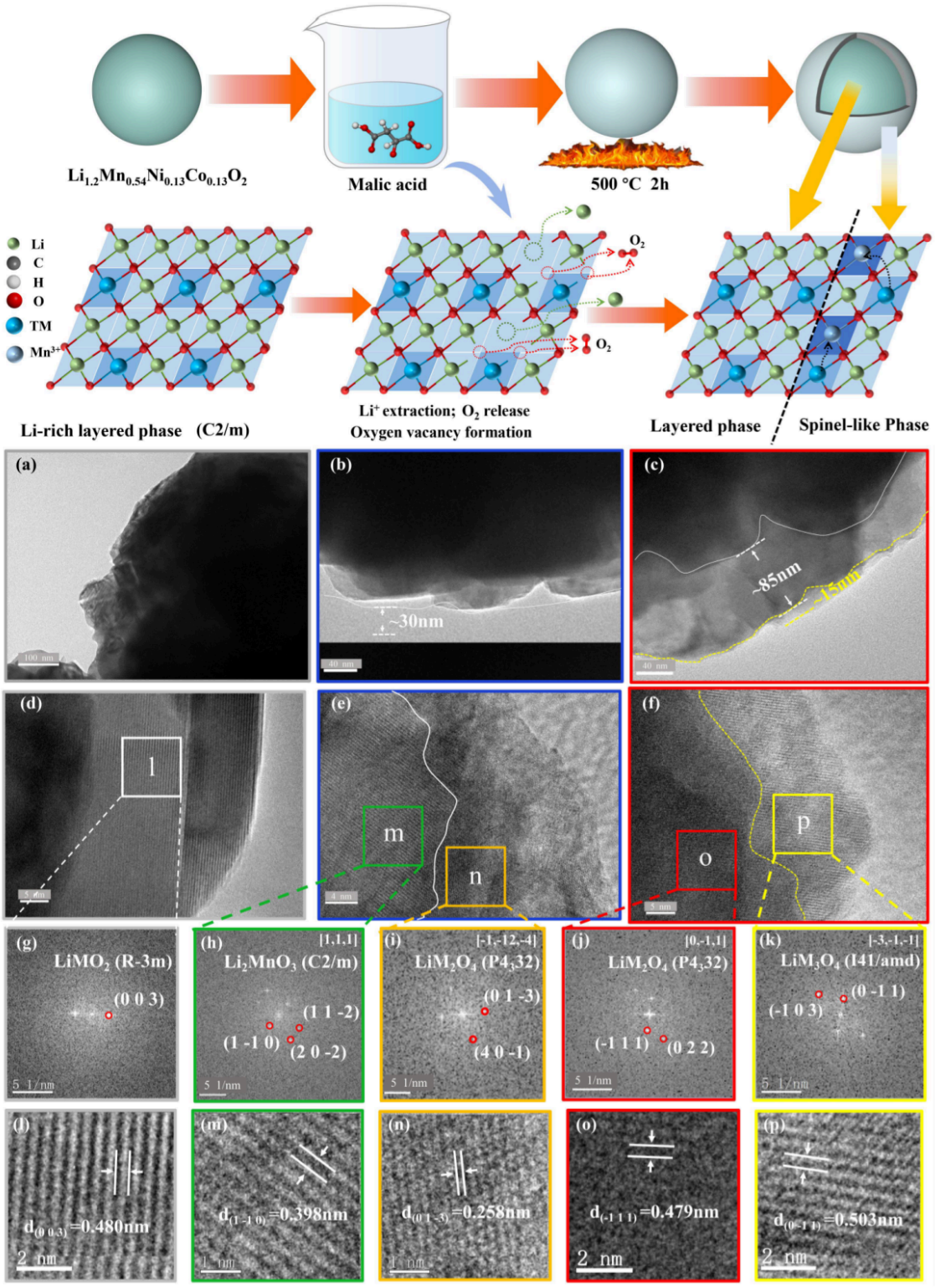

**Figure 1**

(a) XRD patterns and enlarged (003) and (104) reflections; (b) Rietveld refinement of pristine LMR; (c) Rietveld refinement of LMR-2.5@1.




## Figure 2

(a–c) SEM images of the samples; (d–f) elemental mapping; (g–i) EDS spectra.




## Figure 3

Schematic illustration of oxygen vacancy construction and spinel phase formation via acid treatment, along with TEM images of samples subjected to acid leaching at different pH values. For LMR (a, d, g, l), LMR-2.5@1 (b, e, h–i, m–n), and LMR-2.0@1 (c, f, j–o, k–p), the panels show overall morphology, magnified TEM images, corresponding fast Fourier transform (FFT) patterns of selected areas, and further enlarged views of local regions.

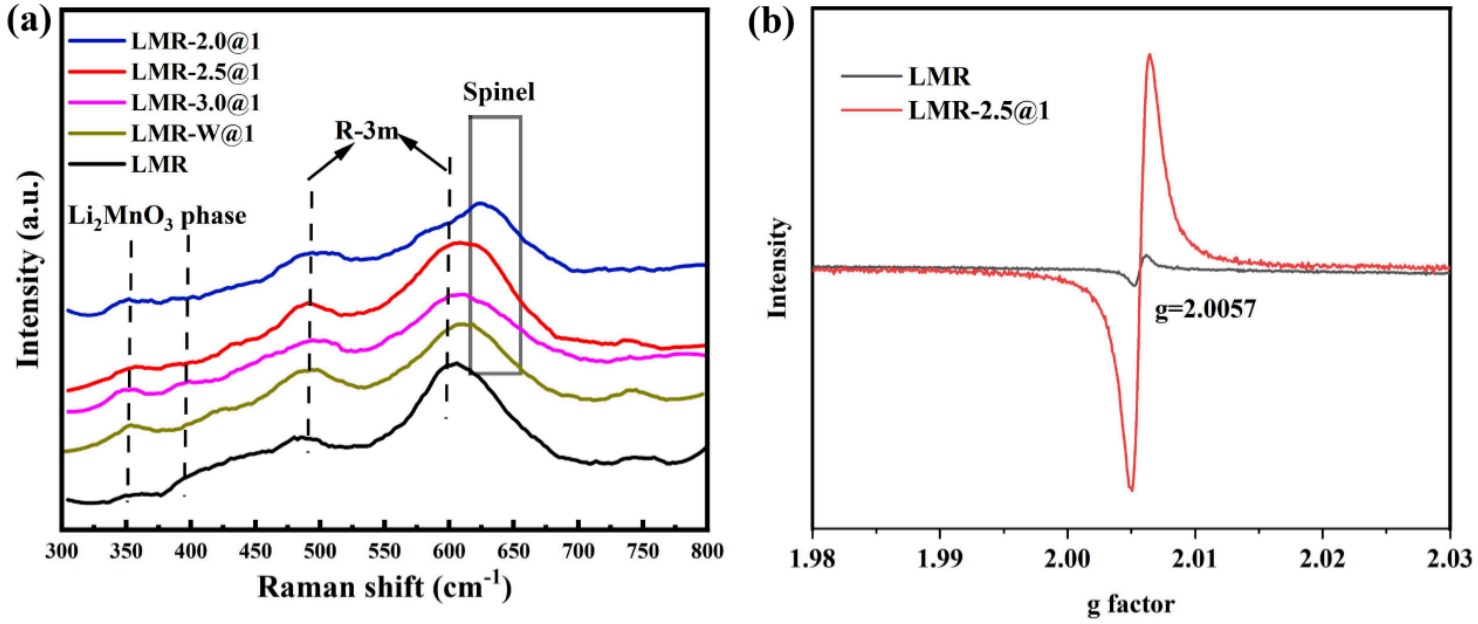



Figure 4

(a) Raman spectra and (b) EPR curves.

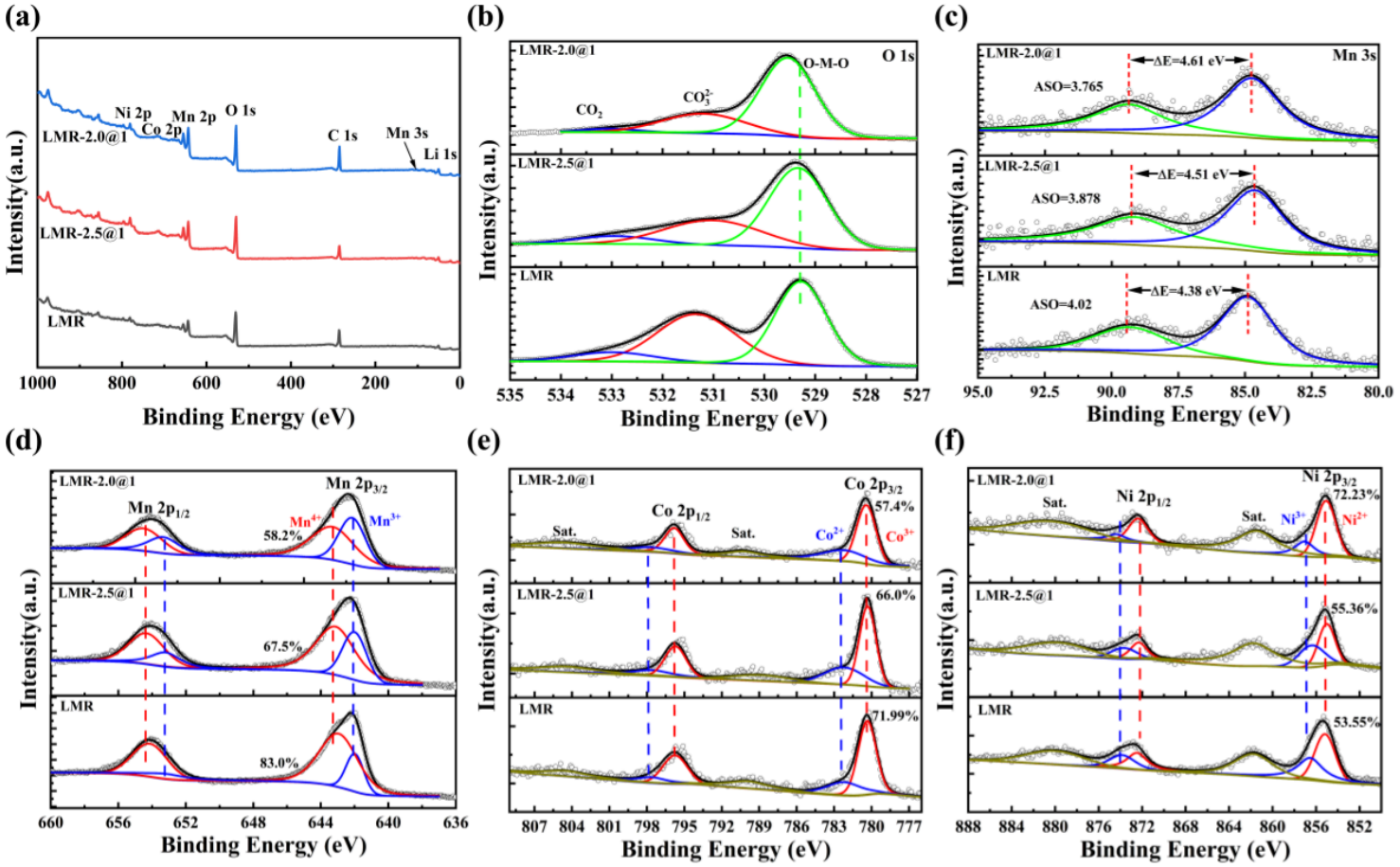
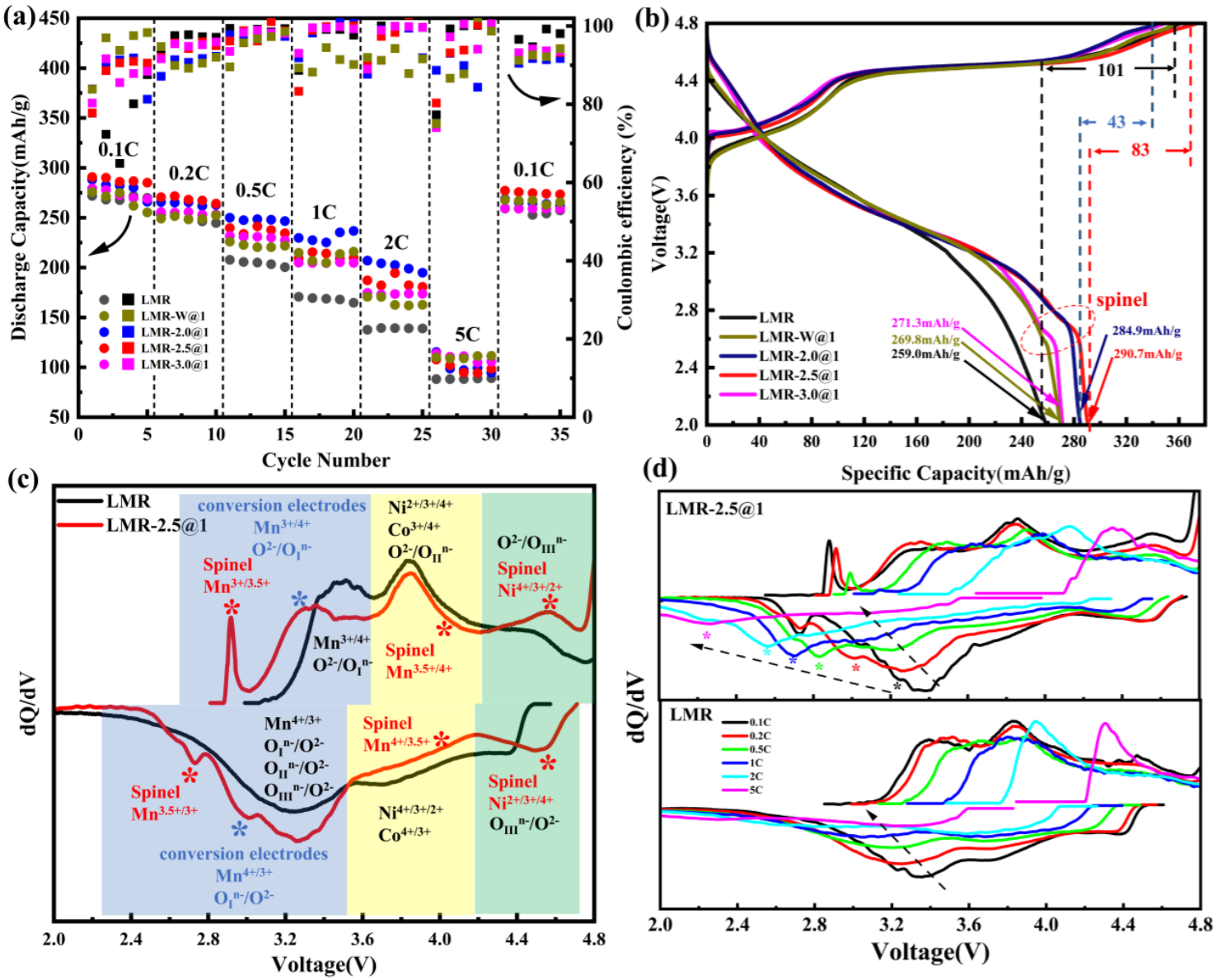


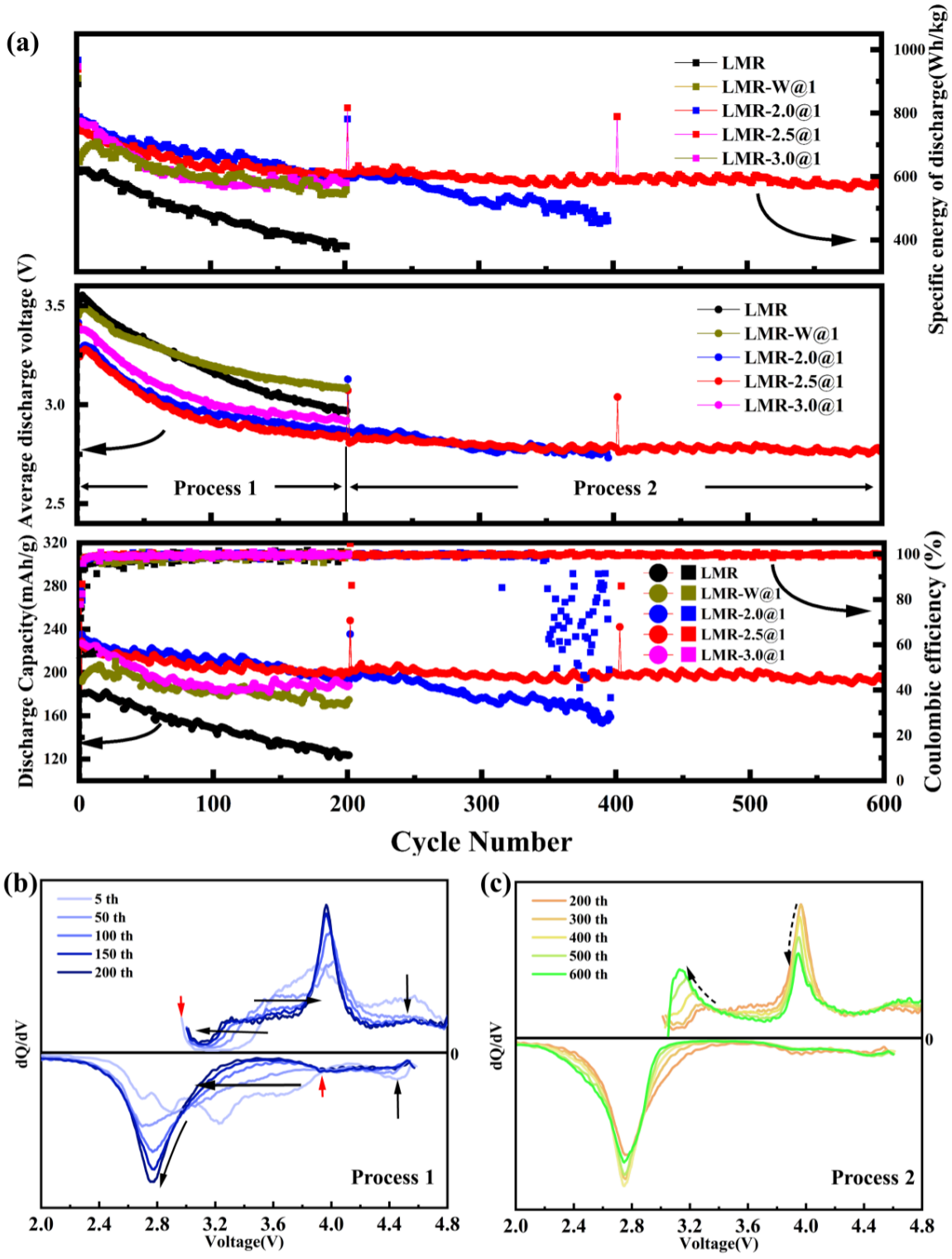

Figure 5

XPS spectra of different samples (a) survey, (b) O 1s, (c) Mn 3s, (d) Mn 2p, (e) Ni 2p, (f) Co 2p.



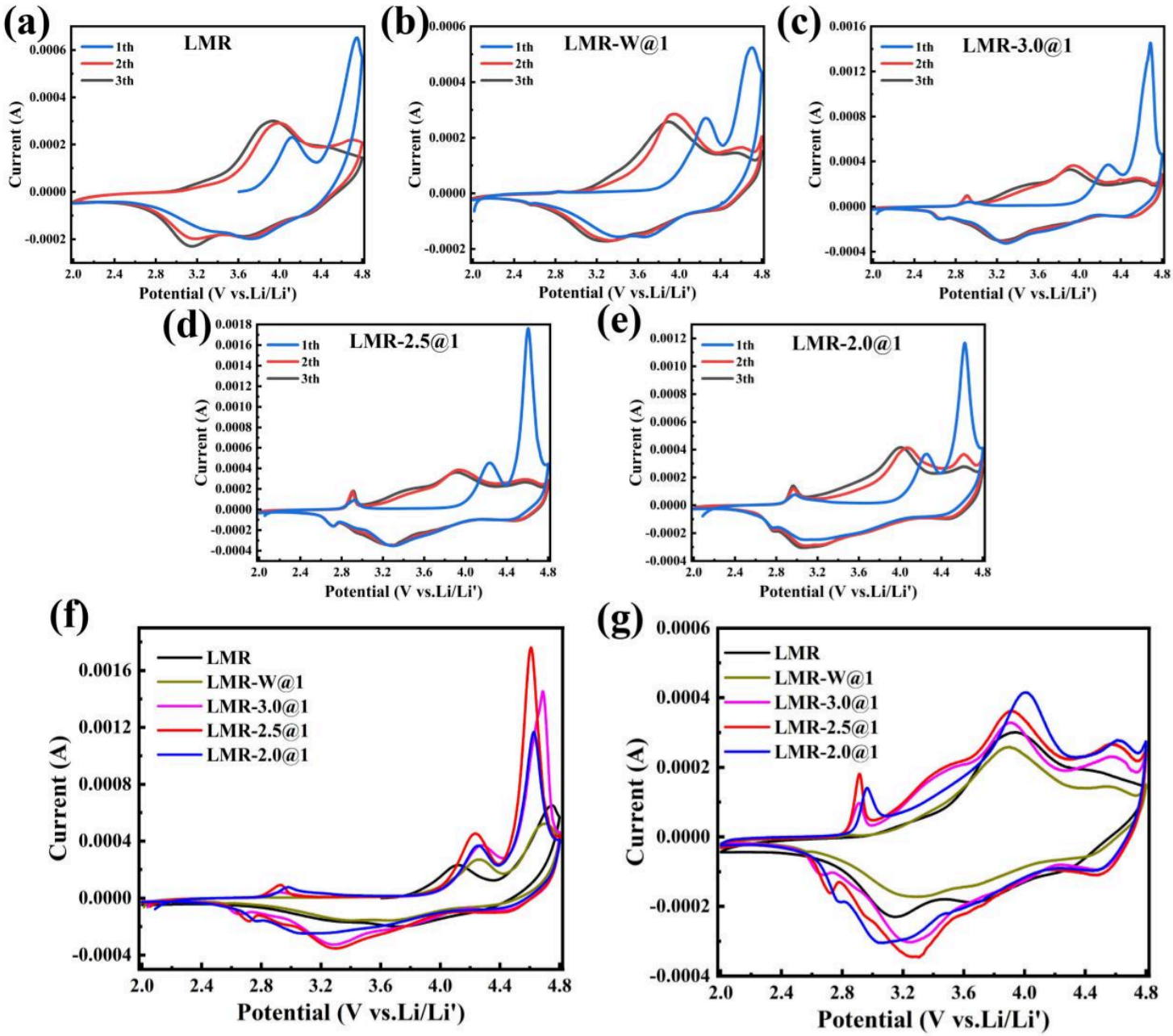

## Figure 6

Electrochemical performance of the samples: (a) rate capability, (b) initial charge–discharge profiles, (c) dQ/dV curves of the first cycle for LMR and LMR-2.5@1, (d) dQ/dV curves at different rates.




## Figure 7

(a) Comparison of galvanostatic charge–discharge data for different samples at 1 C, from bottom to top: discharge specific capacity and Coulombic efficiency, average voltage of discharge curves, and discharge specific energy; (b) dQ/dV curves of LMR-2.5@1 for the first 200 cycles; (c) dQ/dV curves of LMR-2.5@1 for cycles 200 to 600.




## Figure 8

(a-e) Cyclic voltammetry (CV) curves of different samples；(f) the first three cycles of different samples; the first three cycles of different samples; (g) the third-cycle CV curves of different samples.

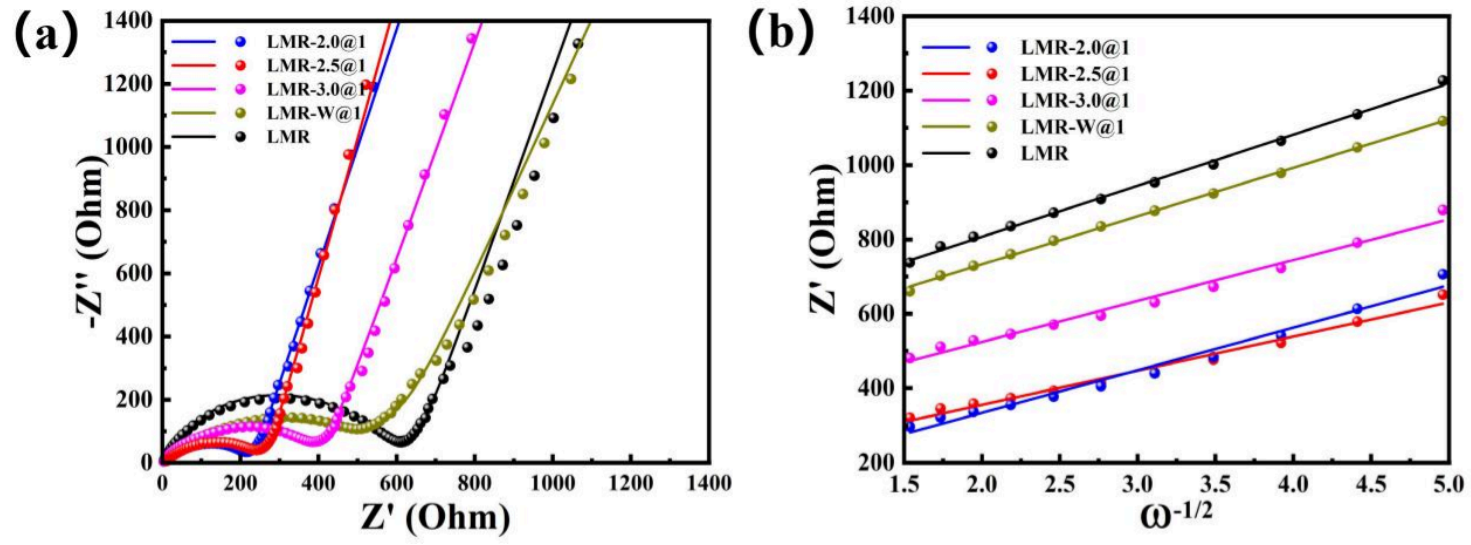



**Figure 9**

(a) EIS spectra of different samples and the corresponding equivalent circuit fitting curves; (b) linear fitting curves of Z' versus the inverse square root of angular frequency ($\omega^{-1/2}$) in the Warburg region.

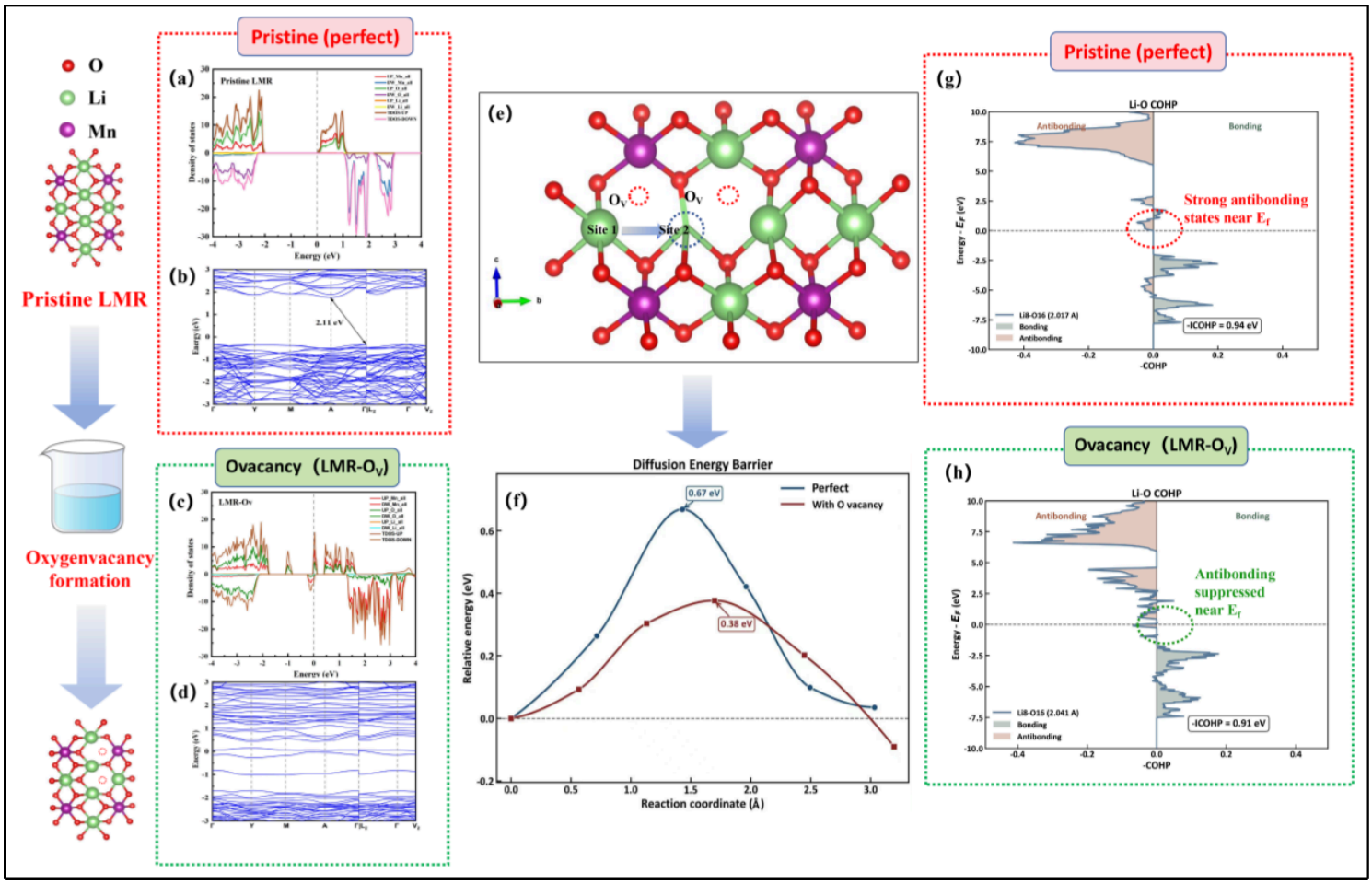



**Figure 10**

(a-b) Density of states and band structure of pristine LMR; (c-d) Density of states and band structure of oxygen-deficient LMR; (e) Model of oxygen vacancy formation and Li-ion migration; (f) Li-ion migration barriers of pristine and oxygen-deficient LMR; (g-h) COHP analysis of Li-O bonding in pristine and oxygen-deficient LMR.